

Deterministic positioning of quantum dots in nanophotonic waveguides

T. Pregolato,¹ X.-L. Chu,¹ T. Schröder,^{1, a)} R. Schott,² A. D. Wieck,² A. Ludwig,² P. Lodahl,^{1, b)} and N. Rotenberg^{1, c)}

¹⁾Center for Hybrid Quantum Networks (Hy-Q), Niels Bohr Institute, University of Copenhagen, Blegdamsvej 17, DK-2100 Copenhagen, Denmark

²⁾Lehrstuhl für Angewandte Festkörperphysik, Ruhr-Universität Bochum, Bochum, Germany

(Dated: 3 September 2022)

The capability to embed quantum dots (QDs) at predefined positions in nanophotonic structures is key to the development of complex quantum photonic architectures. Here, we demonstrate that QDs can be deterministically positioned in nanophotonic waveguides by pre-locating QDs relative to a global reference frame using micro-photoluminescence spectroscopy. After nanofabrication, QD-waveguide misalignments of only (9 ± 46) nm and (1 ± 33) nm are measured, for QDs embedded in undoped and doped membranes, respectively. A priori knowledge of the QD positions allows us to study the spectral changes introduced by nanofabrication. We record average spectral shifts ranging from 0.1 to 1.1 nm only, indicating that the fabrication-induced shifts can generally be compensated by electrical or thermal tuning of the QDs. Finally, we quantify the effects of the nanofabrication on different charge states of the QDs excitons, showing that this change is constant as a function of QD-to-surface separation, down to distances of only 70 nm. These results show that our approach can deterministically integrate QDs into nanophotonic waveguides whose light-fields contain nanoscale structure and whose spectral response varies at the nanometer level, such as photonic crystal waveguides or cavities.

I. INTRODUCTION

The rapid maturation of the InAs quantum dot (QD) platform, and in particular the ability to interface these emitters with high quality nanophotonic structures¹, has opened up viable routes towards the creation of integrated single-photon sources² for quantum network applications^{3,4}. This increasing viability of QD-based photonic technology can be traced to three milestones in the field: the growth of high quality QDs via the Stranski-Krastanov technique⁵, the ability to couple emission from QDs to photonic modes with near-unity efficiency^{6,7}, and the use of doped heterostructures to charge stabilize the environment of the emitters^{8,9}. Altogether, these allow for efficient and highly coherent light-matter interactions⁹⁻¹¹ and the generation of highly-indistinguishable photons^{12,13}, which are basic capabilities of quantum-photonic processing elements.

To date, the vast majority of QD-based devices are fabricated with no *a priori* spatial or spectral knowledge about the emitters. This lack of information results in low yields when QDs are interfaced with nanoscale or dispersive elements such as waveguides or resonators, precluding the scaling up of these systems into complex architectures. Furthermore, without prior knowledge of the QD properties, it has not been possible to quantify the effects of nanofabrication techniques on individual emitters. Recently, a variety of techniques have been developed to address these issues by pre-locating QD positions and then deterministically fabricating photonic structures about their positions. One approach is to use *in-situ* techniques, where cathodoluminescence (CL)¹⁴⁻¹⁶

or micro-photoluminescence (μ PL)^{17,18} spectroscopy first locates the QDs followed by electron-beam or UV lithography to pattern the photonic elements. With CL, QDs were positioned within a nanoscale multimode beam-splitter, with a QD-nanostructure misalignment of only 34 nm¹⁹, while UV lithography defines structures with micron dimensions and therefore does not require the same degree of accuracy.

An alternative approach is to first locate the QDs relative to alignment markers, using either scanning electron microscopy²⁰ or μ PL²¹⁻²³, then fabricate structures in a separate step. Separating the localization and nanofabrication has the distinct advantage of parallelizing the deterministic nanofabrication procedure and is therefore more compatible with the design of time-intensive, complex lithography masks that contain many elements. The images taken in these protocols contain both the *emission* from the QDs and the *reflection* from the alignment markers, yielding typical localization precision at the sub-10 nm level^{24,25}. The reflected image, however, depends on the excitation angle, while the emission pattern from the QDs does not. Hence, slight misalignment of the excitation beam introduces alignment errors, which are reflected in the much-larger QD-nanostructure misalignments found. For example, final QD-nanostructure misalignment of the order of 50 nm has been achieved in nanoguides²⁶ or photonic crystal cavities²², rising to 100's of nanometers for larger devices such as micro-pillars^{25,27} or circular Bragg cavities²³.

Alignment precision on a sub-wavelength scale is generally required in nanophotonics devices where the electromagnetic field is strongly confined and varies spatially. For photonic crystal waveguides, for example, the relevant length scale is the Bragg wavelength inside the medium. This corresponds to QD emission wavelength in the medium of $\lambda/2 \sim 125$ nm for a typical QD emission wavelength of 910 nm. In more quantitative terms, an alignment precision of 50 nm in a photonic-crystal waveguide implies that a photonic coupling efficiency $\geq 96\%$ can be achieved deterministically²⁸.

Here, we present a quantitative and statistical study of the

^{a)}Currently at: Department of Physics, Humboldt-Universität zu Berlin, Newtonstr. 15, 12489 Berlin, Germany

^{b)}Electronic mail: lodahl@nbi.ku.dk

^{c)}Electronic mail: nir.rotenberg@nbi.ku.dk

alignment of pre-located QDs to nanoscale photonic waveguides, using a straightforward improvement to the existing μ PL protocols. Our method results in a systematic misalignment of 9 and 1 nm, randomly distributed with standard deviations of 46 and 33 nm, for samples where the QDs cannot and can be electrically controlled. We furthermore study the effect of fabricating quasi-one-dimensional nanophotonic waveguides or two-dimensional photonic-crystal waveguides (PhCWs) on the spectral response of the QDs, and on the different exciton complexes.

II. PRELOCALIZATION OF QUANTUM DOTS

In this work we set out to achieve a final QD-nanostructures alignment better than 50 nm. To do so we take the following steps: (i) Fabrication of a grid of alignment markers on top of a wafer containing QDs; (ii) Localization of QDs within each grid square and measurement of the spectral properties; (iii) Fabrication of nanostructures at preselected positions. To localize the QDs, in step (ii), we modify the protocol of Liu *et al.*²⁴ in a manner that yields the desired final accuracy. We use only photoluminescence, and not reflection, to image both the alignment markers and the QDs.

Our global coordinate frame is set by a grid of gold crosses, which we fabricate on top of a GaAs membrane with embedded InAs QDs, as shown in Fig. 1a. In this study, we use two types of wafers: the QDs are embedded either within an undoped GaAs membrane that is 160-nm thick, or within a p-i-n diode¹². In either case, each square within the grid is $40\ \mu\text{m}$ by $40\ \mu\text{m}$ and is identified by a binary label (set of small gold rectangles fabricated with different orientations). We also fabricate a grid of solid gold lines that we use to quantify and correct for the rotation of our images (not shown).

We locate the position of the QDs within each square of the grid in two steps, first imaging the crosses and then finding the QDs, all at a cryogenic temperature of about 10K. Examples of these two images are shown in panels II and III of Fig. 1a. Although the excitation scheme does not change – namely we use above band excitation at 780 nm, illuminating in wide-field configuration an area slightly larger than the square – our imaging protocol depends on the type of wafer used. In either case we image the reference markers and the QDs separately, using emission from the sample in both cases, and not via the reflected laser light. Consequently, no alignment errors are introduced due to slight angles of the excitation beam. This improvement simplifies the measurement, and, as we show below, decreases the final misalignment between the QDs and nanostructures below previously reported values.

For the intrinsic sample, we use an 800 nm long-pass filter to block the reflected laser light, using the luminescence of the GaAs membrane to image our reference markers (using an Andor iKon-M camera). As shown in Fig. 1a, panel II, the gold markers block the light emitted by the GaAs and therefore appear as shadows in the resultant image. By fitting a line to each arm of the crosses, we find their centers, typically with an accuracy of 3.1 nm that is largely determined by the signal-to-noise ratio of the measurement. This value is far

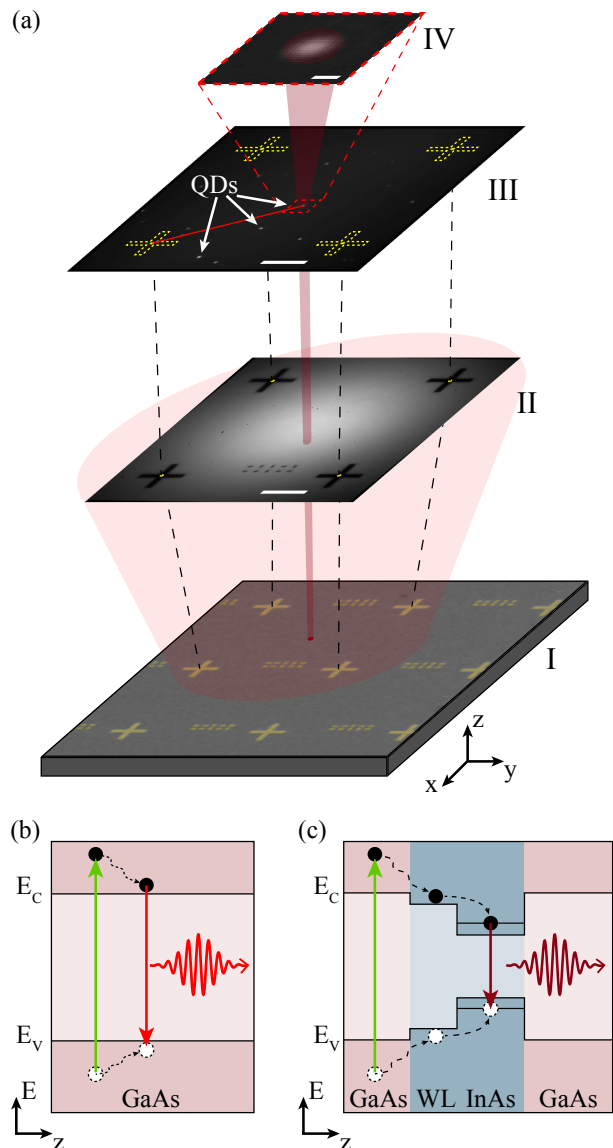


FIG. 1. Prelocalization protocol for epitaxially grown QDs (real data shown). (a) I: False color SEM of the GaAs membrane with embedded InAs QDs, with a gold alignment mask of crosses. II: First the alignment mask is imaged and the crosses located, using the photoluminescence of the membrane, as discussed in the main text. III: The QD photoluminescence is imaged and spatially correlated with the cross positions. As example, we point to several QDs. IV: Closed-up image of the emission pattern of a single QD. All scalebars are $10\ \mu\text{m}$ in length, except for IV, where it is 500 nm long. Energy levels of the GaAs membrane (b) and embedded QD and wetting layer WL (c). In both cases, above band illumination (green arrow) and subsequent fast, non-radiative decay (black arrows) excites an electron (black symbol) to the conduction band, leaving a hole (white symbol) in the valence band of the GaAs or QD. Recombination of the electron and hole results in the emission of a photon, whose wavelength is typically near 830 - 850 nm and 930 nm for the membrane and QDs (light and dark red arrows, respectively).

below the diffraction limit of the setup, and is typical of what

is reported in the literature²⁴.

Taking separate images of the alignment markers and QDs has an additional advantage. To locate the QDs, a narrowband ($935 \text{ nm} \pm 0.5 \text{ nm}$) filter is placed in the collection path, blocking the emission from the GaAs, resulting in background-free images as shown in panel III of Fig. 1a. We then fit a two-dimensional Gaussian to each QD, finding its location to within 0.6 nm that, due to the higher signal to background ratio, is an order of magnitude smaller than the value reported in current state-of-the-art literature²⁴. Assuming that our field-of-view is unchanged between these two images, we find the position of each QD relative to the global reference frame with an accuracy of 4.8 nm.

The ability to electrically control the optical properties of the QD on the gated sample allows us to further improve the localization protocol, a change that ultimately leads to better QD-structure alignment accuracy (see Sec. III). Here, the QDs are embedded in a diode with a large built-in field, meaning that the energy levels are strongly tilted relative to those of Fig. 1c. Consequently, in this natural state (i.e. with no applied bias voltage) the excited electrons quickly tunnel out of the QD, and no emission is observed. Conversely, we can ‘turn on’ the QDs by applying a bias voltage to recover the configuration of Fig. 1c²⁹. This electrical control allows imaging both the crosses and the QDs, independently, without changing filters but rather by tuning the applied voltage, ensuring that our field-of-view is constant. To do so, a 900 nm long-pass filter is placed in the collection path, blocking the relatively strong emission from the GaAs, which would otherwise swamp the signal from the QDs. Instead, we use the tail end of the emission from the wetting layer to image the crosses with the QDs ‘off’, when we do not apply a bias voltage. In these images we find the position of the center of each cross with an accuracy of 5.5 nm. We then apply 500 mV to turn on the QD emission, which then dominates over the wetting layer fluorescence. The resultant image can be used to localize the emitters’ positions to within 0.7 nm. As before, by correlating the two images we find the absolute position of each QD with an accuracy of 9.2 nm. We note that this value, which is consistent with earlier reports^{24,25}, is below the level of overlay accuracy ($\pm 15 \text{ nm}$) that our e-beam lithography system (Elionix ELS-F125) can achieve.

After localization, and if desired, additional measurements can be made using pre-selected QDs. Here, for example, we switch to a confocal setup, where we can excite each QD individually and record its emission spectrum (see Sec. IV below). Similarly, the lifetime or single-photon purity of each emitter can be quantified before fabrication.

III. DETERMINISTIC INTEGRATION OF QUANTUM DOTS INTO NANOPHOTONIC WAVEGUIDES

The important figure-of-merit for the deterministic integration of solid-state emitters into nanophotonic elements is not the precision with which the emitters are located relative to a reference frame, but rather the final alignment between the emitters and the nanostructures. We therefore fab-

ricate nanophotonic waveguides³⁰ at the predetermined positions of selected QDs, as shown in Fig. 2a, making both quasi-one-dimensional nanoguides and two-dimensional PhCWs. The nanoguides have a rectangular cross-sections with widths ranging from 288 to 631 nm. The PhCWs are created by removing a row of holes from photonic crystals with lattice constants ranging from 233 nm to 247 nm and hole radii ranging from 71 nm to 76 nm, and are fabricated with QDs at different positions within the photonic crystal unit cell (i.e. distances to the nearest surface), as we discuss below.

Micro-photoluminescence measurements on the waveguides after fabrication allow us to determine whether they contain the targeted QD and to subsequently quantify the misalignment between the emitters and waveguides. The yield of the undoped sample, which contains 48 nanoguides and 50 PhCWs is 96% and 92% for the two types of structures, respectively. In contrast, the yield of the doped sample is 93% and 74% for the nanoguides and PhCWs, respectively. To understand the low yield of the doped PhCW structures we further break down the data by target distance of the QDs from the nearest surface, finding a yield of 94% when this distance is $\geq 100 \text{ nm}$ but only 44% for distances $< 100 \text{ nm}$. In contrast, for the undoped sample, the yield was 80% for distances $< 100 \text{ nm}$, despite having a relatively higher misalignment, as we show below. We can understand this difference as follows: The area near a lateral surface – in our case the holes of the PhCW – is known to have a reduced electrical conductivity due to a local depletion of the free carriers³¹. Hence we are unable to properly apply a bias voltage to QDs that are located in these regions, in contrast to QDs at similar separations from the hole surface in the undoped sample (which are always ‘on’). Regardless, we note that for both types of samples we succeeded in observing emission from QDs nominally positioned within about 30 nm of a hole edge.

The actual misalignment between QD and nanostructure for each sample was quantified from images of the photoluminescence from the nanoguides, as shown in the inset to Fig. 2b. In these images, the nanoguides, whose width is below the resolution of our optical system, appear as a one-dimensional Gaussian profile. By fitting this Gaussian we find the center of the waveguide, which we mark with the dashed line in the inset to Fig. 2b. Similarly, we find the position of the QD using a two-dimensional Airy function (center denoted by the red dot in Fig. 2), allowing to quantify the final misalignment Δ between the two. A histogram of Δ for QDs embedded in the nanoguides on the intrinsic wafer is shown in Fig. 2b, along with the fitted normal distribution, from which we find a misalignment of $(9 \pm 46) \text{ nm}$. We attribute the slight mean misalignment of 9 nm to a rigid shift introduced during the nanofabrication, which is within the 15 nm layer alignment accuracy of the electron beam lithography system. The spread of the distribution (46 nm standard deviation) mainly arises from imperfections within our imaging system, for example a beam-offset introduced by the bandpass filter that allows us to measure emission from the QDs. To “successfully” couple the QD to a nanophotonic structure we require the total error to be smaller than the size of the features in its light field. Our total error, we note, is sufficiently small to enable excellent²⁸

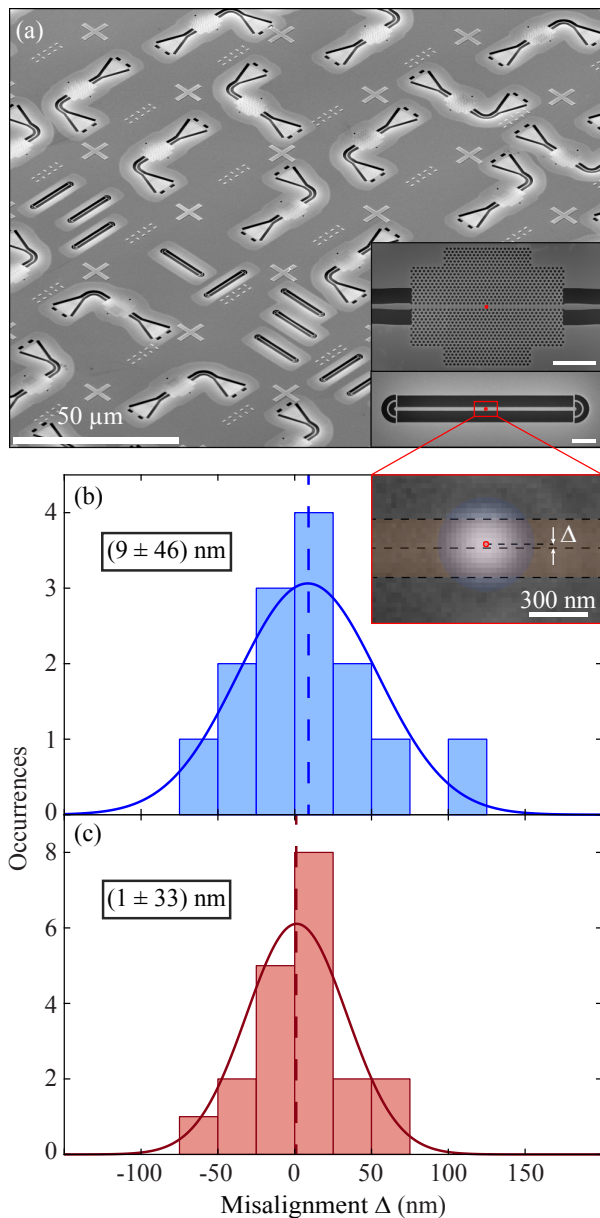


FIG. 2. Nanophotonic waveguides fabricated about pre-located QDs. (a) A representative area of the resultant photonic chips with both nanoguides and photonic crystal waveguides containing QDs (see inset, scalebars are both $2 \mu\text{m}$). (b) Measured misalignment distribution between the QDs and the center of a nanoguide for the intrinsic sample. The mean and standard deviation are given. The inset shows a false-color μPL image where the edges and center of the nanoguide are marked by dashed lines, the QD emission is shown in blue with the center denoted by the red dot, and the relative misalignment indicated by Δ . (c) Same as in (b) but for the doped sample. The smaller misalignment spread in (c) is attributed to the removal of the bandpass filter used in the localization of the QDs on the undoped sample, which ensures that both the QD and reference images are taken with the exact same field of view.

coupling to a PhCW.

A similar analysis of the nanoguides on the doped sample

reveals the benefit of taking all images using the same filter. The misalignment histogram for this sample, which we show in Fig. 2c, reveals a Δ of only (1 ± 33) nm. That is, in this case we observe a vanishing average systematic shift of the alignment, and a smaller spread in the misalignment relative to that of the undoped sample. We attribute this improvement to using the same physical imaging optics for both alignment and QD frames.

IV. EFFECTS OF NANOFABRICATION

With the notable exception of a study comparing the linewidth of QDs before and after integration into a micropillar cavity³², there have been no studies of the way the spectral properties of individual QDs change when they are integrated into nanostructures. To address this need, we record the fluorescence spectra from the QDs before and after nanofabrication, for both types of wafers by optically exciting them from the top. For the QDs in the doped samples, we maintain the same bias voltage of 300 mV before and after nanofabrication.

Exemplary spectra of the same QD in bulk and in a nanoguide, here in an undoped wafer, are shown in Fig. 3a. For this QD, we observe a clear shift $\Delta\lambda \approx 1$ nm, which is a typical value for this wafer and this structure. In fact, from the histogram of such shifts (Fig. 3b) we calculate a mean $\Delta\lambda = (0.8 \pm 0.6)$ nm. Similar data for the QDs in PhCWs reveal a smaller $\Delta\lambda = (0.1 \pm 0.7)$ nm (Fig. 3c). In fact, shifts of this order of magnitude are consistent with changes to the stress and strain within the GaAs membrane due to the removal of the sacrificial layer³³ and the different values of $\Delta\lambda$ for the two types of structures may arise from their different dimensionalities and material compositions.

We perform similar experiments and analysis on the QDs embedded in nanophotonic waveguides on the doped samples. In this case, we measure $\Delta\lambda = (-0.2 \pm 0.3)$ nm and (-1.1 ± 0.6) nm for the QDs embedded in the nanoguides and PhCWs, respectively (Figs. 3d and e). Although these shifts are of the same magnitude as those in the intrinsic sample, they are now in the opposite direction, demonstrating that the fabrication process affects the layered and homogeneous wafers in a different manner.

The spectral shifts presented in Fig. 3 can be further subdivided according to nanoguide width or emitter position within the unit cell for the PhCWs. The results, presented in Fig. 4, demonstrate that in either case the shift is constant to within the measurement error. This means that, for the nanoguides (Fig. 4a), there is no appreciable difference to $\Delta\lambda$ between QDs that are 144 nm away from the waveguide wall and those with a separation of 315.5 nm. This is likewise true for the QDs in the PhCWs, regardless of whether the QD was shifted in x or y along the unit cell (Figs. 4b and c, respectively), although a larger $\Delta\lambda$ is observed for the doped sample. Here, the separation between the QDs and the nearest edge of the PhCWs varied between about 29 and 171 nm. The uniformity of these shifts allows us to conclude that they do not arise due to the presence of surfaces, for example due to the trapping of charges, but rather supports the notion that their origin can be

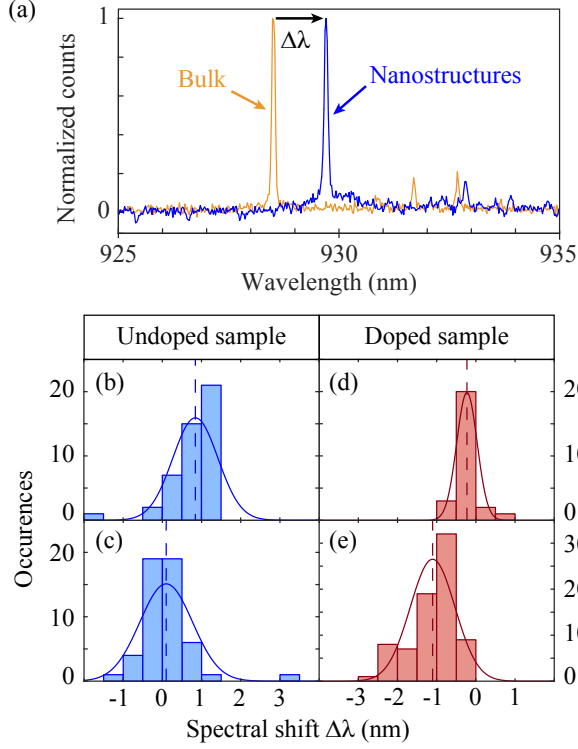


FIG. 3. Effects of nanofabrication on the spectral properties of QDs. (a) Emission spectra for a QD both before nanofabrication (bulk sample) and after when it is embedded in a nanoguide. Each spectra is normalized to its respective maximum, and the spectral shift $\Delta\lambda$ is marked. (b) and (c) Histograms of spectral shifts for QDs embedded in nanobeam and PhCWs, respectively, in undoped samples. Also shown are the fitted normal distributions from which we extract the mean $\Delta\lambda$ for each set of structures. (d) and (e) Same as in (b) and (c) but for the doped wafer, with all spectra taken at an applied $V = 300$ mV.

traced to the general relaxation of the GaAs membrane due to the removal of the sacrificial AlGaAs layer.

Encouragingly, the fabrication-induced shifts can be largely overcome through the electrical gating of the QDs in the doped sample. This can be seen in the μ PL spectra, taken with above-band excitation for different applied bias voltages, an example of which is shown in Fig. 5. Here the charge plateaus for both the neutral (X^0) and charged (X^+) excitons are displayed both in bulk and after integration into a PhCW. The charged exciton is identified as positively charged because it appears at lower applied bias voltages (i.e. larger fields) than the neutral excitonic line^{12,34}. For both excitons, we observe a blue-shift of the emission wavelength due to the nanofabrication, whose statistics were captured in Fig. 3e. It is clear that, for this QD, increasing the applied bias by about 150 mV recovers the bulk emission wavelength over a fairly broad bandwidth of ≈ 0.6 and 0.5 nm for X^0 and X^+ , respectively.

By fitting the Stark shift of the QD as is done in Fig. 5a (dashed lines), we quantify the effects of the nanofabrication on the emitter dipole. This model describes the quadratic de-

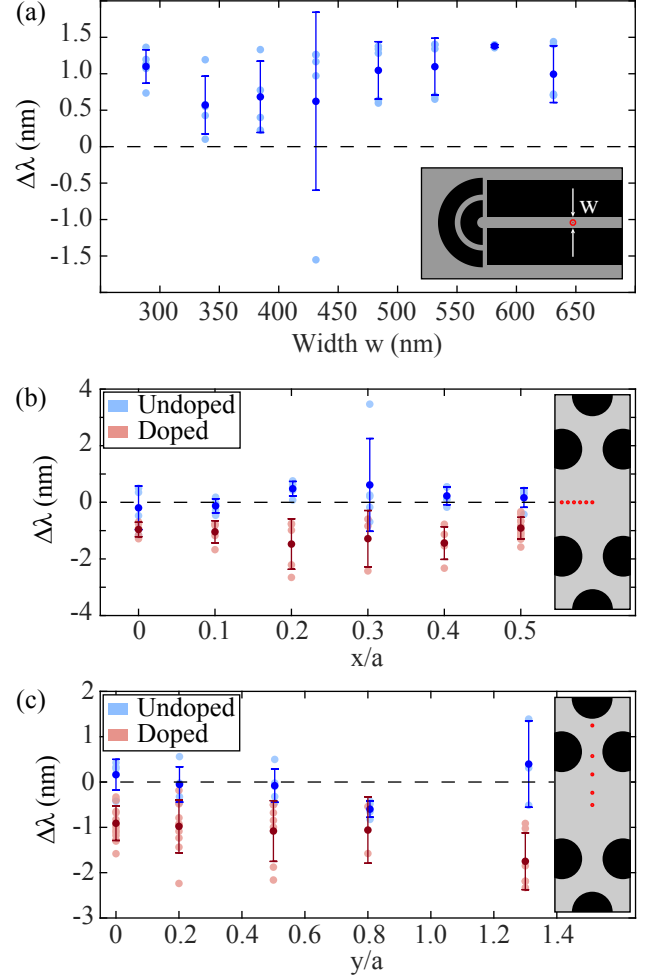


FIG. 4. Dependence of the spectral shift of QD resonances due to integration in (a) nanoguides of various sizes and (b) and (c) different positions within PhCWs. The dark colored symbols and error bars are the mean and standard deviation of $\Delta\lambda$, with the corresponding individual measurements shown by the faded circles. The inset to (a) shows the width of the nanoguide, while in (b) and (c) the positions of the QDs within the unit cell of the PhCW are depicted.

pendence of the Stark shift on the transition energy^{35–37}, written in the terms of emission wavelength as

$$\frac{hc}{\lambda} = \frac{hc}{\lambda_0} - p_z F + \alpha F^2. \quad (1)$$

Here, λ_0 is the QD emission wavelength at vanishing applied field, p_z is the permanent dipole moment of the QD in the growth direction, α is the polarizability of the emitter, and $F = (V - V_i)/t$ is the applied field for a given bias voltage V . The thickness of the intrinsic layer surrounding the QDs is nominally $t = 70$ nm and the built-in field has been calculated from the difference between the Fermi levels of the p- and n-doped GaAs layers³⁸, resulting $V_i/t = 224.24$ kV/cm. The fit parameters for the 4 excitonic lines shown in Fig. 5a are given in Fig. 5b, and are comparable with values reported in literature^{36,37,39,40}.

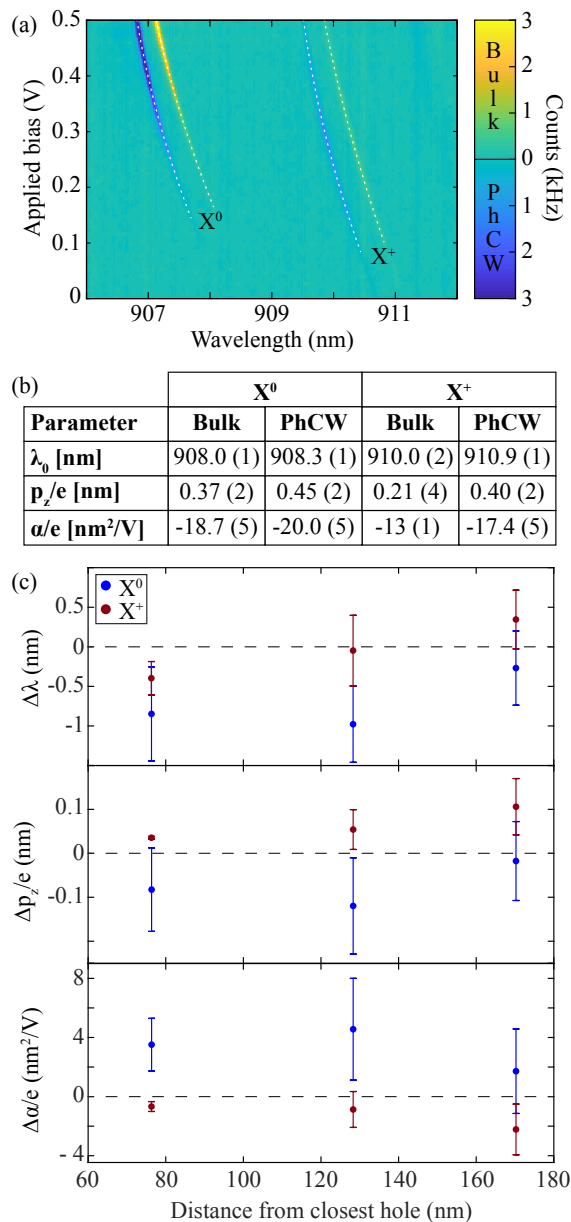


FIG. 5. Electrical tuning of QDs before and after fabrication of a PhCW. (a) Voltage-wavelength PL spectra for a QD located 170 nm away from the nearest surface of a PhCW. The fluorescence plateaus of both the neutral (X^0) and charged (X^+) excitons are seen in the maps and, in this exemplary case, both blue shift by about 0.3 nm with applied bias. The curvature of the plateaus, however, changes differently, revealing that the nanofabrication affects the two excitons differently. These changes can be quantified via a theoretical model (dashed line), as discussed in the main text. (b) Fit parameters for the different excitons shown in (a). (c) Nanofabrication induced changes to the Stark-shift parameters as a function of nominal distance to the nearest surface. Two to four QDs were measured at each position of the PhCW unit cell, and the error bars represent the calculated standard deviation.

We analyze similar frequency-voltage spectral maps for QDs located at different positions within the PhCW unit cell,

quantifying possible fabrication induced changes to the dipole parameters. The results are presented in Fig. 5c. This analysis reveals that the effects of the nanofabrication on the charged exciton are generally small compared to the changes of X^0 . This observation may be related to the different exciton wavefunctions associated with neutral and charged excitons where the former is further extended than the latter³⁶, therefore possibly making it more susceptible to the local environment. We also note that no pronounced dependence on the distance of the QDs from the etched holes are observed, which indicates once again that strain and stress alterations rather than surface defects may be responsible for the observed spectral changes.

V. CONCLUSIONS AND OUTLOOK

We have presented a method for precisely locating epitaxially grown QDs that allows us to deterministically integrate the emitters into nanostructured photonic waveguides. A statistical analysis of μ PL images after fabrication reveals systematic misalignments of below 10 nm and with corresponding random errors less than 50 nm. The obtained precision suffices next-generation quantum nanophotonics experiments with waveguides and cavities, such as mapping out the spatial dependence of the optical local density of states or precisely probing the spatial polarization profile of nanophotonic waveguides leading to chiral emission⁴¹. Combined with the demonstrated spectral control via Stark tuning, a path is laid out towards the deterministic coupling of multiple QDs via the engineered dipole-dipole interaction through the waveguide. Such controlled interaction may be applied for two-qubit gates between emitting QDs, enabling the generation of advanced photonic quantum resources such as 2D clusters of multiple entangled photons⁴².

ACKNOWLEDGMENTS

The authors gratefully acknowledge Sandra Ø. Madsen for her help in the construction of the optical setup and Leonardo Midolo and Zhe Liu for assistance in fabrication. We gratefully acknowledge financial support from the Danish National Research Foundation (Center of Excellence “Hy-Q”), the Europe Research Council (ERC Advanced Grant “SCALE”), the European Union’s Horizon 2020 research and innovation program under the Marie Skłodowska Curie grant agreement no. 753067 (OPHOCS), Innovation Fund Denmark (Quantum Innovation Center “Qubiz”), and the Danish Research Infrastructure Grant (QUANTECH).

¹P. Lodahl, S. Mahmoodian, and S. Stobbe, “Interfacing single photons and single quantum dots with photonic nanostructures,” *Rev. Mod. Phys.* **87**, 347–400 (2015).

²A. J. Shields, “Semiconductor quantum light sources,” *Nat. Photonics* **1**, 215–223 (2007).

³J. Borregaard, A. S. Sørensen, and P. Lodahl, “Quantum Networks with Deterministic Spin-Photon Interfaces,” *Adv. Quantum Technol.*, 1800091 (2019).

⁴P. Lodahl, “Quantum-dot based photonic quantum networks,” *Quantum Sci. Technol.* **3**, 013001 (2018).

- ⁵P. M. Petroff, A. Lorke, and A. İmamoğlu, “Epitaxially self-assembled quantum dots,” *Phys. Today* **54**, 46–52 (2001).
- ⁶M. Arcari, I. Söllner, A. Javadi, S. Lindskov Hansen, S. Mahmoodian, J. Liu, H. Thyrestrup, E. H. Lee, J. D. Song, S. Stobbe, and P. Lodahl, “Near-Unity Coupling Efficiency of a Quantum Emitter to a Photonic Crystal Waveguide,” *Phys. Rev. Lett.* **113**, 093603 (2014).
- ⁷X. Ding, Y. He, Z.-C. Duan, N. Gregersen, M.-C. Chen, S. Unsleber, S. Maier, C. Schneider, M. Kamp, S. Höfling, C.-Y. Lu, and J.-W. Pan, “On-Demand Single Photons with High Extraction Efficiency and Near-Unity Indistinguishability from a Resonantly Driven Quantum Dot in a Micropillar,” *Phys. Rev. Lett.* **116**, 020401 (2016).
- ⁸A. V. Kuhlmann, J. H. Prechtel, J. Houel, A. Ludwig, D. Reuter, A. D. Wieck, and R. J. Warburton, “Transform-limited single photons from a single quantum dot,” *Nat. Commun.* **6**, 8204 (2015).
- ⁹M. C. Löbl, I. Söllner, A. Javadi, T. Pregolato, R. Schott, L. Midolo, A. V. Kuhlmann, S. Stobbe, A. D. Wieck, P. Lodahl, A. Ludwig, and R. J. Warburton, “Narrow optical linewidths and spin pumping on charge-tunable close-to-surface self-assembled quantum dots in an ultrathin diode,” *Phys. Rev. B* **96**, 165440 (2017).
- ¹⁰H. Thyrestrup, G. Kiršanskė, H. Le Jeannic, T. Pregolato, L. Zhai, L. Raa-hauge, L. Midolo, N. Rotenberg, A. Javadi, R. Schott, A. D. Wieck, A. Ludwig, M. C. Löbl, I. Söllner, R. J. Warburton, and P. Lodahl, “Quantum Optics with Near-Lifetime-Limited Quantum-Dot Transitions in a Nanophotonic Waveguide,” *Nano Lett.* **18**, 1801–1806 (2018).
- ¹¹P. Türschmann, H. L. Jeannic, S. F. Simonsen, H. R. Haakh, S. Götzinger, V. Sandoghdar, and N. Rotenberg, “Coherent nonlinear optics of quantum emitters in nanophotonic waveguides,” (2019), arXiv:1906.08565.
- ¹²G. Kiršanskė, H. Thyrestrup, R. S. Daveau, C. L. Dreeßen, T. Pregolato, L. Midolo, P. Tighineanu, A. Javadi, S. Stobbe, R. Schott, A. Ludwig, A. D. Wieck, S. I. Park, J. D. Song, A. V. Kuhlmann, I. Söllner, M. C. Löbl, R. J. Warburton, and P. Lodahl, “Indistinguishable and efficient single photons from a quantum dot in a planar nanobeam waveguide,” *Phys. Rev. B* **96**, 165306 (2017).
- ¹³Y.-M. He, Y. He, Y.-J. Wei, D. Wu, M. Atatüre, C. Schneider, S. Höfling, M. Kamp, C.-Y. Lu, and J.-W. Pan, “On-demand semiconductor single-photon source with near-unity indistinguishability,” *Nat. Nanotechnol.* **8**, 213–217 (2013).
- ¹⁴M. Gschrey, F. Gericke, A. Schübler, R. Schmidt, J.-H. Schulze, T. Heindel, S. Rodt, A. Strittmatter, and S. Reitzenstein, “In situ electron-beam lithography of deterministic single-quantum-dot mesa-structures using low-temperature cathodoluminescence spectroscopy,” *Appl. Phys. Lett.* **102**, 251113 (2013).
- ¹⁵M. Gschrey, R. Schmidt, J.-H. Schulze, A. Strittmatter, S. Rodt, and S. Reitzenstein, “Resolution and alignment accuracy of low-temperature in situ electron beam lithography for nanophotonic device fabrication,” *J. Vac. Sci. Technol. B, Nanotechnol. Microelectron. Mater. Process. Meas. Phenom.* **33**, 021603 (2015).
- ¹⁶A. Kaganskiy, M. Gschrey, A. Schlehahn, R. Schmidt, J.-H. Schulze, T. Heindel, A. Strittmatter, S. Rodt, and S. Reitzenstein, “Advanced in-situ electron-beam lithography for deterministic nanophotonic device processing,” *Rev. Sci. Instrum.* **86**, 073903 (2015).
- ¹⁷A. Dousse, J. Suffczynski, R. Braive, A. Miard, A. Lemaître, I. Sagnes, L. Lanco, J. Bloch, P. Voisin, and P. Senellart, “Scalable implementation of strongly coupled cavity-quantum dot devices,” *Appl. Phys. Lett.* **94**, 121102 (2009).
- ¹⁸M. Sartison, S. L. Portalupi, T. Gissibl, M. Jetter, H. Giessen, and P. Michler, “Combining in-situ lithography with 3D printed solid immersion lenses for single quantum dot spectroscopy,” *Sci. Rep.* **7**, 39916 (2017).
- ¹⁹P. Schnauber, J. Schall, S. Bounouar, T. Höhne, S.-I. Park, G.-H. Ryu, T. Heindel, S. Burger, J.-D. Song, S. Rodt, and S. Reitzenstein, “Deterministic Integration of Quantum Dots into on-Chip Multimode Interference Beamsplitters Using In Situ Electron Beam Lithography,” *Nano Lett.* **18**, 2336–2342 (2018).
- ²⁰A. Badolato, K. Hennessy, M. Atatüre, J. Dreiser, E. Hu, P. M. Petroff, and A. İmamoğlu, “Deterministic coupling of single quantum dots to single nanocavity modes,” *Science* **308**, 1158–61 (2005).
- ²¹S. M. Thon, M. T. Rakher, H. Kim, J. Gudat, W. T. M. Irvine, P. M. Petroff, and D. Bouwmeester, “Strong coupling through optical positioning of a quantum dot in a photonic crystal cavity,” *Appl. Phys. Lett.* **94**, 111115 (2009).
- ²²T. Kojima, K. Kojima, T. Asano, and S. Noda, “Accurate alignment of a photonic crystal nanocavity with an embedded quantum dot based on optical microscopic photoluminescence imaging,” *Appl. Phys. Lett.* **102**, 011110 (2013).
- ²³L. Sapienza, M. Davanço, A. Badolato, and K. Srinivasan, “Nanoscale optical positioning of single quantum dots for bright and pure single-photon emission,” *Nat. Commun.* **6**, 7833 (2015).
- ²⁴J. Liu, M. I. Davanço, L. Sapienza, K. Konthasinghe, J. V. De Miranda Cardoso, J. D. Song, A. Badolato, and K. Srinivasan, “Cryogenic photoluminescence imaging system for nanoscale positioning of single quantum emitters,” *Rev. Sci. Instrum.* **88**, 023116 (2017).
- ²⁵Y.-M. He, J. Liu, S. Maier, M. Emmerling, S. Gerhardt, M. Davanço, K. Srinivasan, C. Schneider, and S. Höfling, “Deterministic implementation of a bright, on-demand single-photon source with near-unity indistinguishability via quantum dot imaging,” *Optica* **4**, 802 (2017).
- ²⁶R. J. Coles, D. M. Price, J. E. Dixon, B. Royall, E. Clarke, P. Kok, M. S. Skolnick, A. M. Fox, and M. N. Makhonin, “Chirality of nanophotonic waveguide with embedded quantum emitter for unidirectional spin transfer,” *Nat. Commun.* **7**, 11183 (2016).
- ²⁷S. Liu, Y. Wei, R. Su, R. Su, B. Ma, Z. Chen, H. Ni, Z. Niu, Y. Yu, Y. Wei, X. Wang, and S. Yu, “A deterministic quantum dot micropillar single photon source with >65% extraction efficiency based on fluorescence imaging method,” *Sci. Rep.* **7**, 13986 (2017).
- ²⁸A. Javadi, S. Mahmoodian, I. Söllner, and P. Lodahl, “Numerical modeling of the coupling efficiency of single quantum emitters in photonic-crystal waveguides,” *J. Opt. Soc. Am. B* **35**, 514 (2018).
- ²⁹P. W. Fry, J. J. Finley, L. R. Wilson, A. Lemaître, D. J. Mowbray, M. S. Skolnick, M. Hopkinson, G. Hill, and J. C. Clark, “Electric-field-dependent carrier capture and escape in self-assembled InAs/GaAs quantum dots,” *Appl. Phys. Lett.* **77**, 4344 (2000).
- ³⁰L. Midolo, T. Pregolato, G. Kiršanskė, and S. Stobbe, “Soft-mask fabrication of gallium arsenide nanomembranes for integrated quantum photonics,” *Nanotechnology* **26**, 484002 (2015).
- ³¹A. Berrier, M. Mulot, G. Malm, M. Östling, and S. Anand, “Carrier transport through a dry-etched InP-based two-dimensional photonic crystal,” *J. Appl. Phys.* **101**, 123101 (2007).
- ³²J. Liu, K. Konthasinghe, M. Davanço, J. Lawall, V. Anant, V. Verma, R. Mirin, S. W. Nam, J. D. Song, B. Ma, Z. S. Chen, H. Q. Ni, Z. C. Niu, and K. Srinivasan, “Single Self-Assembled InAs/GaAs Quantum Dots in Photonic Nanostructures: The Role of Nanofabrication,” *Phys. Rev. Appl.* **9**, 064019 (2018).
- ³³T. Nakaoka, T. Kakitsuka, T. Saito, S. Kako, S. Ishida, M. Nishioka, Y. Yoshikuni, and Y. Arakawa, “Strain-induced modifications of the electronic states of InGaAs quantum dots embedded in bowed airbridge structures,” *J. Appl. Phys.* **94**, 6812–6817 (2003).
- ³⁴P. A. Dalgarno, J. M. Smith, J. McFarlane, B. D. Gerardot, K. Karrai, A. Badolato, P. M. Petroff, and R. J. Warburton, “Coulomb interactions in single charged self-assembled quantum dots: Radiative lifetime and recombination energy,” *Phys. Rev. B* **77**, 245311 (2008).
- ³⁵P. Fry, I. Itskevich, D. Mowbray, M. Skolnick, J. Finley, J. Barker, E. O’Reilly, L. Wilson, I. Larkin, P. Maksym, M. Hopkinson, M. Al-Khafaji, J. David, A. Cullis, G. Hill, and J. Clark, “Inverted Electron-Hole Alignment in InAs-GaAs Self-Assembled Quantum Dots,” *Phys. Rev. Lett.* **84**, 733–736 (2000).
- ³⁶J. Finley, M. Sabathil, P. Vogl, G. Abstreiter, R. Oulton, A. Tartakovskii, D. Mowbray, M. Skolnick, S. Liew, A. Cullis, and M. Hopkinson, “Quantum-confined Stark shifts of charged exciton complexes in quantum dots,” *Phys. Rev. B* **70**, 201308 (2004).
- ³⁷A. J. Bennett, R. B. Patel, J. Skiba-Szymanska, C. A. Nicoll, I. Farrer, D. A. Ritchie, and A. J. Shields, “Giant Stark effect in the emission of single semiconductor quantum dots,” *Appl. Phys. Lett.* **97**, 031104 (2010).
- ³⁸S. Sze and K. K. Ng, *Physics of Semiconductor Devices* (John Wiley & Sons, Inc., Hoboken, NJ, USA, 2006).
- ³⁹R. J. Warburton, C. Schulhauser, D. Haft, C. Schäfflein, K. Karrai, J. M. Garcia, W. Schoenfeld, and P. M. Petroff, “Giant permanent dipole moments of excitons in semiconductor nanostructures,” *Phys. Rev. B* **65**, 113303 (2002).
- ⁴⁰T. M. Hsu, W.-H. Chang, C. C. Huang, N. T. Yeh, and J.-I. Chyi, “Quantum-confined Stark shift in electroreflectance of InAs/In_xGa_{1-x}As self-assembled quantum dots,” *Appl. Phys. Lett.* **78**, 1760–1762 (2001).

- ⁴¹P. Lodahl, S. Mahmoodian, S. Stobbe, A. Rauschenbeutel, P. Schneeweiss, J. Volz, H. Pichler, and P. Zoller, “Chiral quantum optics,” *Nature* **541**, 473–480 (2017). X 7, 041023 (2017).
- ⁴²D. Buterakos, E. Barnes, and S. E. Economou, “Deterministic Generation of All-Photonic Quantum Repeaters from Solid-State Emitters,” *Phys. Rev.*